Journal of Alloys and Compounds 509 (2011) 9617–9626

Contents lists available at ScienceDirect

Journal of Alloys and Compounds

journal homepage: www.elsevier.com/locate/jallcom

Effect of the sintering temperature on the properties of nanocrystalline $Ca_{1-x}Sm_xMnO_3$ ($0 \leq x \leq 0.4$) powders

I. Matos [a], S. Sério [b], M.E. Lopes [c], M.R. Nunes [d], M.E. Melo Jorge [d,*]

[a] Departamento de Química e Bioquímica, Faculdade de Ciências, Universidade de Lisboa, Portugal
[b] CEFITEC, Departamento de Física, Faculdade de Ciências e Tecnologia da Universidade Nova de Lisboa, Portugal
[c] Departamento de Química, Centro de Química de Évora, Universidade de Évora, Évora, Portugal
[d] Departamento de Química e Bioquímica, Centro de Ciências Moleculares e Materiais, Faculdade de Ciências, Universidade de Lisboa, Portugal

ARTICLE INFO

Article history:
Received 6 May 2011
Received in revised form 10 July 2011
Accepted 11 July 2011
Available online 23 July 2011

Keywords:
Nanocrystalline manganites
Citrate gel method
Samarium substituted
Rietveld analysis
Electrical properties

ABSTRACT

Nanocrystalline $Ca_{1-x}Sm_xMnO_3$ ($0 \leq x \leq 0.4$) manganites were prepared by a soft chemical method (Pechini method) followed by auto-combustion and sintering in air at 1073 or 1473 K. Single-phase powders with general composition $Ca_{1-x}Sm_xMnO_3$ were obtained after 18 h annealing. The particle and grain sizes of the substituted Sm-manganites did not exhibit variation with samarium content, but increase with increasing the sintering temperature. All manganites show two active IR vibrational modes near 400 and 600 cm^{-1} characteristic of the BO_6 octahedron vibrations.

For the samples sintered at T_s = 1473 K, the partial substitution of calcium by samarium in the $CaMnO_3$ phase induces a marked decrease in the electrical resistivity, in the temperature range of 300–900 K, and at the same time a metal-to-insulator transition occurs; for T_s = 1073 K all the samples present semiconductor behaviour. With the increase of the annealing temperature the grain size increases and a metal–semiconductor transition appears. The results can be ascribed to the Mn^{4+}/Mn^{3+} ratio and particle grain size. The effects of particle size on the electrical properties can be attributed to the domain status, changes in the Mn–O–Mn bond angle and Mn–O bond length.

1. Introduction

Perovskites and related compounds are widely investigated because some of them exhibit fascinating properties like metal–insulator (MI) transitions, charge ordering and ferromagnetism. Although the focus of interest has mostly rested in the hole-doped manganites $Ln_{1-x}A_xMnO_3$ (Ln = La-Tb, and A = Ca, Sr, Ba, Pb, etc.) due to their potential applications [1–6], many researchers have placed emphasis on electron-doped perovskite manganites with the general formula $Ca_{1-x}Ln_xMnO_3$ (Ln-rare earth ion) [7–12]. One of these oxides that raised enormous interest is $Ca_{1-x}Sm_xMnO_3$, where Ca^{2+} is partially replaced by the trivalent rare earth cation, Sm^{3+}. Doping with electrons introduces mobile electrons into the e_g band and consequently the interaction of these carriers via t_{2g} spins induces changes in the electrical and magnetic properties. The electron-doped manganites $Ca_{1-x}Sm_xMnO_3$ have been recently investigated [13–18] by electrical resistivity, thermoelectric power, magnetic susceptibility, thermal conductivity, X-ray, neutron and electron diffractions and microscopy techniques. Traditionally, the electron-doped perovskite phases $Ca_{1-x}Sm_xMnO_3$ have been prepared by solid-state reactions, between the corresponding oxides or carbonates, at high temperature. This method generally generates inhomogeneous products. Phase formation often requires heating at temperature, of the order of 1573 K or above for prolonged periods, leading to powders with a high grain size and a small surface area. In recent years, nanomaterials have attracted considerable attention because of their unique chemical, catalytic, electrochemical, electronic, optical and mechanical properties. Several techniques, based on solution chemistry methods, have been employed for the preparation of highly homogeneous fine powders of these perovskite oxide materials using low processing temperatures in comparison with the conventional solid state reaction process [19–27].Gel combustion method combines the advantages of the chemical sol–gel process and the low-temperature combustion process. This preparation method is quite simple and leads to homogeneous, highly reactive and nanosized powders. Accordingly single-phase perovskite powders can be produced at low temperature and the product physical properties can be improved. This preparation route, developed in recent years, has been tested in different ceramic compounds and applied to synthesize several materials with perovskite-type structure [20–27]. It is widely accepted that the performance of the perovskite oxide materials strongly depends on chemical

* Corresponding author at: Departamento de Química e Bioquímica FCUL, Campo Grande C8, 1749-016 Lisboa, Portugal.
E-mail addresses: mebmj@fc.ul.pt, mdjorge@fc.ul.pt (M.E.Melo Jorge).

0925-8388/$ – see front matter © 2011 Elsevier B.V. All rights reserved.
doi:10.1016/j.jallcom.2011.07.032

homogeneity, particle size and morphology of the oxide materials. Therefore, the challenge of improving the preparation method and controlling the grain size still remains.

Some authors [24,25] have shown that the substitution of calcium by cerium or holmium in the $Ca_{1-x}R_xMnO_3$ system, prepared by citrate route in the temperature range 1173–1533 K, induces a marked decrease in the electrical resistivity and a metal–insulator transition at high temperature. More recently, nanocrystalline $Ca_{1-x}R_xMnO_{3-\delta}$ manganites (R = Ho, Eu) were synthesized as single-phase by a simple and instantaneous solution auto gel combustion method at low temperature, namely 1073 K for 18 h. These studies showed that all samples exhibit semiconductor behaviour. Also the resistivity at room temperature and the activation energy for electrical conduction (E_a) display an important correlation with the crystal structure and the particle grain size [26,27].

In the present work, $Ca_{1-x}Sm_xMnO_{3-\delta}$ $(0 \le x \le 0.4)$ samples were synthesized by the soft chemical method (the Pechini method). This method is known to be effective for the preparation of fine perovskite powders at low temperature. The reactive fine powders obtained by the decomposition of the corresponding polymeric organic metal compounds are expected to be suitable raw materials for preparing the Sm doped calcium manganites at low temperatures in air. The effect of particle size and samarium content on the structure, morphology and electrical properties at high temperature of $Ca_{1-x}Sm_xMnO_{3-\delta}$ $(0 \le x \le 0.4)$ were investigated. Furthermore, a detailed structural analysis at room-temperature was performed, since there are no published data on the detailed crystalline structure, namely Rietveld structural parameters, bond lengths and bond angles for the Mn octahedron (except for $Ca_{0.9}Sm_{0.1}MnO_3$ phase prepared by conventional solid-state reaction method at 1623 K [16] and 1773 K [17]). Also, the $Ca_{1-x}Sm_xMnO_3$ system electrical behaviour at high temperature range has not been yet explored, excluding the phase with $x = 0.1$ [16]. Therefore the present studies will provide, for the first time, results of these important properties.

2. Experimental

Single-phase nanocrystalline samples of $Ca_{1-x}Sm_xMnO_3$ $(0 \le x \le 0.4)$ were synthesized by the sol–gel process. Appropriate amounts of $CaCO_3$ (Merck), Sm_2O_3 previously heated at 1173 K during 8 h (Aldrich) and $Mn(NO_3)_2{\cdot}4H_2O$ (Riedel-de Haën, p.a.) were separately dissolved in a HNO_3 solution (Riedel-de Haën). The solutions of calcium, samarium and manganese were mixed and an amount of citric acid (Riedel-de Haën) equivalent to the total number of moles of metal ions was added under moderate heating and stirring conditions. Temperature was raised to 390–420 K, to promote polymerization and remove the solvents. The solution became more viscous and the colour changed from yellow to brown with the formation of a large amount of gases (nitrogen and carbon oxides). The mixture ignited and got on fire resulting in a voluminous combustion product. The self-propagating combustion was complete within a few seconds, giving rise to a brownish-black ash material. The decomposition of most of the organic carbon residue was performed in a sand bath at 673 K for about 2–3 h and after it was heated at 873 K, for 6 h, in a furnace. The resin became a black solid mass and the obtained material was pulverized, using an agate mortar and pestle, before further treatment. Thermal treatments were performed in air atmosphere at 1073 and 1473 K for 18 h, each heating with intermediate grindings in alumina crucibles (Alsint 99.7), to produce samples with different particle sizes.

Assuming complete combustion, the proposed equation for the formation of the samples with $x = 0.3$ is as follows:

$$0.7Ca(NO_3)_2(aq) + 0.3Sm(NO_3)_3(aq) + Mn(NO_3)_2(aq) + C_6H_8O_7(aq) + 1.8O_2 \rightarrow Ca_{0.7}Sm_{0.3}MnO_3(s) + 6CO_2(g) + 0.2NO_2(g) + 4.1NO(g) + 4H_2O(g)$$

The powders structural characterization was carried out for all samples at room temperature by XRD using a Philips PW 1730 X-ray powder diffractometer, operating with monochromatized Cu-K_α radiation in Bragg–Brentano geometry. Full profile fitting refinements of the final powder diffraction data in the range $20^\circ \le 2\theta \le 120^\circ$ with a scan rate of 0.02° and a count time of 20 s per step were performed using the program FULLPROF [28], based on the Rietveld method.

The average crystallite sizes of the powders were determined by X-ray line broadening using the Scherrer formula [29].

FTIR spectra were registered with a Nicolet 6700-FTIR equipment, using KBr as powder diluent. The spectra were the result of averaging out 64 scans obtained at room temperature in the 4000–350 cm^{-1} range.

In order to determine the oxygen content and the average manganese oxidation state of the manganite powders, iodometric titrations were performed. Around 50 mg of sample was accurately weighed in a flask and an excess of solid potassium iodide, KI, (Riedel-de Haën), relatively to the Mn^{4+} and Mn^{3+} amounts in the sample, was added. After that concentrated HCl (Merck) was added to dissolve the mixture KI-sample and the solution titrated with sodium thiosulfate volumetric standard (Merck). Near the endpoint 3 drops of starch was added as an indicator. All samples can be considered stoichiometric within the experimental error (±0.01). Consequently, the effects arising from oxygen or cation vacancies must be negligible.

The morphology and the particle size of the calcined powders were observed by scanning electron microscope Jeol JSM-5610LV (SEM). Prior to analysis, a thin layer of Au was evaporated onto the SEM specimens to increase the surface electrical conductivity.

The electrical resistivity of all samples was measured by the standard four-point method from 300 K up to 900 K on sintered pellets prepared under a constant pressure of 50 mbar.

3. Results and discussion

3.1. Phase formation

Fig. 1 shows representative X-ray diffractograms for $Ca_{0.6}Sm_{0.4}MnO_3$ phase. The X-ray diffraction pattern of the sample heated at 873 K indicates that a perovskite phase, with a slightly amorphous background was formed. As the calcination temperature is increased up to 1073, the samples crystallinity improves and a better definition of the XRD peak shape is observed. This effect is further enhanced with the heat treatment at 1473 K. The temperature of 873 K is much lower than those that have been reported for the formation of the perovskite phase employing the traditional ceramic method [13–18].

Fig. 2 presents the different stages of the Sm-substituted manganites $Ca_{0.6}Sm_{0.4}MnO_3$ formation by means of FTIR analysis. The very strong and broad band at ca. 1425 cm^{-1} can be assigned to the asymmetric and symmetric C–O stretching vibrations of ionized carboxylate [30]. These ions are also responsible for the band at ca. 876 cm^{-1}. This means that the hydrogen atoms from carboxyl group of the citric acid were replaced by the metal cations to form a citrate complex. These absorption bands totally disappear from the calcined product at 1073 and 1473 K, showing that

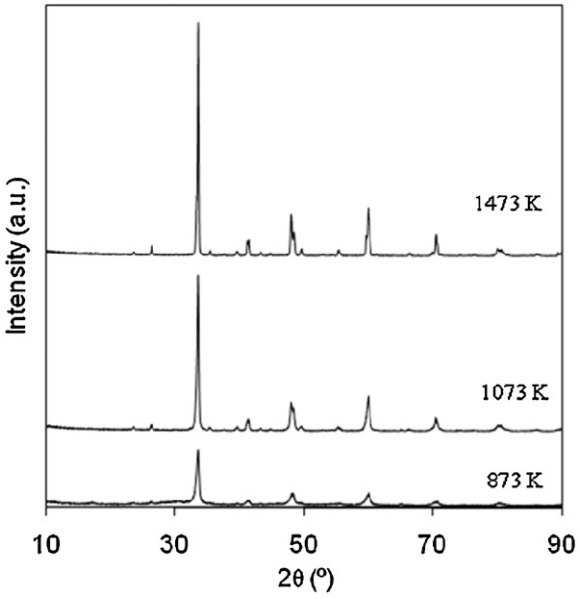

Fig. 1. X-ray diffraction patterns of $Ca_{0.6}Sm_{0.4}MnO_3$ powders produced by gel-combustion synthesis after heat treatments at several temperatures.

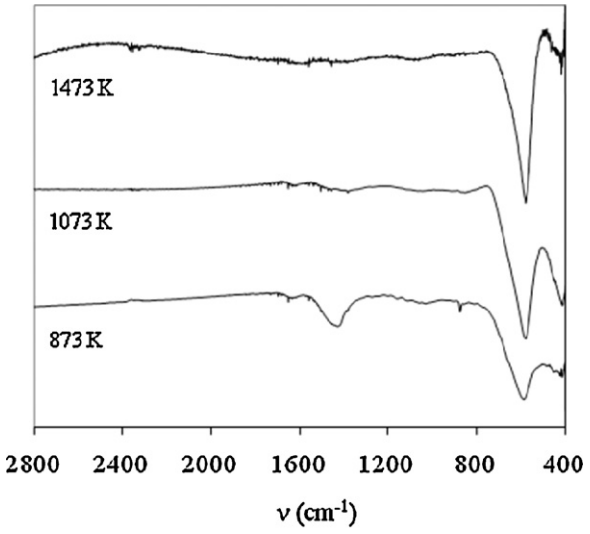

Fig. 2. Infrared spectra of the $Ca_{0.6}Sm_{0.4}MnO_3$ powders produced by gel-combustion synthesis after heat treatments at several temperatures.

the citric acid and the citrate complex components are completely eliminated at these stages but not at the first stage of the decomposition. The products resulting from the heat treatments at 1073 and 1473 K present much simpler IR spectra with just two strong bands at ca. 600 and 400 cm^{-1} characteristics of the perovskite structure [31,32]. These two bands are also visible for the sample heated at 873 K, as expected from X-ray diffractogram.

So, although the X-ray diffraction patterns for the calcined powder at 873 K confirm the presence of a single phase, the FTIR spectra allowed us to conclude that the lower calcination temperature to get the single phase compound without amorphous impurities is 1073 K. Therefore our further studies exclude the samples heated at 873 K and involves only those sintered at T_s = 1073 and 1473 K. We believe that $Ca_{1-x}Sm_xMnO_{3-\delta}$ phases are formed at a relatively low temperature, 1073 K, due to the high reactivity of the homogeneously dispersed ultrafine ash and also the rapid release of thermal energy during the combustion process that characterizes this synthesis route.

3.2. Powder X-ray diffraction and structure

The systematic investigation of the $Ca_{1-x}Sm_xMnO_3$ oxides using XRD shows that they are single phase with an orthorhombic-perovskite structure $GdFeO_3$-type cell, i.e., all the Bragg peaks were completely indexed using an orthorhombic unit cell with $a \approx c \approx a_p\sqrt{2}$ and $b \approx 2a_p$, space group *Pnma* (#62) at room temperature (a_p is the parameter of the cubic perovskite subcell). The structural parameters were determined by Rietveld refinement method. The data were first analyzed with a "whole pattern fitting" algorithm in order to determine accurately the profile shape function, background and the cell parameters. This preliminary study provided a good estimation of R_{WP} and χ^2 that could be reached during the structure refinement. In the refinements, the background was fitted with a 6-term polynomial function, the profiles were modelled using a pseudo-Voigt profile shape function and two asymmetry parameters were used.

The initial positional parameters were taken from previous reported data of the $CaMnO_3$ phase [24,30]. In order to perform the structure refinement it was considered that the ions were statistically distributed on the different crystallographic sites and the occupancy factors were fixed according to the sample stoichiometry. The isotropic temperature factors were fixed at 0.01 $Å^2$. This analysis was also carried out for x = 0 sample. Some results for

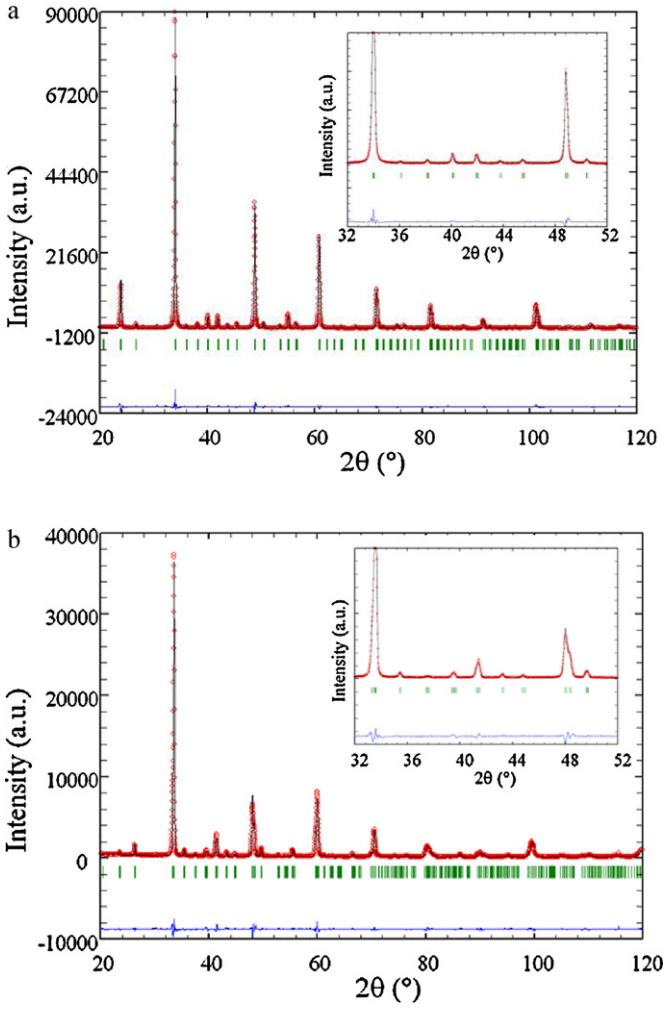

Fig. 3. Rietveld refinement results for $CaMnO_3$ (a) and $Ca_{0.6}Sm_{0.4}MnO_3$ (b) prepared at 1473 K. The experimental data points are shown as dots, and the calculated fit and difference curve are shown as solid lines. Tick marks indicate the calculated reflection positions. The inset shows a zoom in the region between 32–52° (2θ). (a) x = 0.00, (b) x = 0.25.

the phase prepared at 1073 K have been already reported [26,27]. Fig. 3 presents the X-ray diffraction patterns for two representative members of the series $Ca_{1-x}Sm_xMnO_3$ with x = 0 and x = 0.4 synthesized at 1473 K, including the observed and calculated diffraction profiles and the difference between them. The refined structural parameters are listed in Table 1. The selected bond distances Mn–O and Mn–O–Mn bond angles, obtained from the refined atomic positions, together with the MnO_6 octahedron distortion for each sample at room temperature are reported in Table 2. The data indicate that there are no significant differences in the calculated structural parameters as a function of synthesis temperature. The slight decrease in the calculated error observed with the increase of the synthesis temperature may be associated with the better definition of the diffraction peaks obtained for higher heating temperatures.

The Bragg reflections are sharp and symmetric confirming the excellent composition homogeneity of the samples, namely for the phases prepared at 1473 K. For both synthesis temperatures a clear variation is detected in all three cell parameters: a, $b/\sqrt{2}$ and c increase with samarium content (as example see Fig. 4 for the phases synthesized at 1473 K and Table 1). It can readily be observed that the relation $b/\sqrt{2} < c < a$ is valid and the orthorhombic cell can be referred as O'-type structure [33], which can be originated by the strong cooperative Jahn–Teller effect due

Table 1
Refined structural parameters of $Ca_{1-x}Sm_xMnO_3$ ($0 \le x \le 0.4$) at room temperature and the orthorhombicity values (Or). The space group *Pnma* was used and apical oxygen O1a occupy the 4c (x, 1/4, z) site, Mn the 4b (0, 0, 1/2) site and the plane oxygen O1p the general 8d (x, y, z) site.

T_s (K)	x		0	0.1	0.2	0.3	0.4
1073	a (Å)		5.2781 (2)	5.3028 (2)	5.3277 (3)	5.3502 (3)	5.3889 (3)
	b (Å)		7.4542 (3)	7.4769 (3)	7.4965 (3)	7.5066 (4)	7.5343 (4)
	c (Å)		5.2758 (2)	5.2871 (2)	5.3068 (3)	5.3221 (3)	5.3450 (2)
	V (Å^3)		207.57 (1)	209.62 (2)	211.95 (2)	213.90 (2)	217.02 (2)
	Or[a] (%)		0.022	0.148	0.196	0.263	0.409
	Ca/Eu	x	0.0302 (1)	0.0310 (1)	0.03318 (1)	0.0318 (1)	0.0360 (1)
		z	−0.0114 (1)	−0.0106 (1)	−0.0099 (1)	−0.0098 (1)	−0.0056 (1)
	O1a	x	0.4897 (4)	0.4871 (4)	0.4862 (5)	0.4880 (7)	0.4934 (7)
		z	0.0647 (4)	0.0558 (4)	0.0554 (5)	0.0602 (7)	0.0638 (7)
	O1p	x	0.2900 (3)	0.2929 (4)	0.2913 (5)	0.2925 (5)	0.2930 (5)
		y	0.0332 (3)	0.0342 (4)	0.0351 (5)	0.0323 (5)	0.0314 (5)
		z	−0.2894 (3)	−0.2913 (4)	−0.2911 (5)	−0.2910 (5)	−0.2889 (5)
	R_{WP} (%)		7.07	7.92	10.10	10.7	10.20
	R_B (%)		1.02	1.53	2.11	3.01	2.80
	χ^2 (%)		1.71	1.90	3.01	6.91	3.15
	R_F (%)		1.34	2.00	2.75	4.26	2.61
1473	a (Å)		5.2782 (1)	5.2987 (1)	5.3224 (1)	5.3497 (2)	5.3771 (2)
	b (Å)		7.4562 (2)	7.4763 (1)	7.4990 (2)	7.5168 (2)	7.5305 (3)
	c (Å)		5.2766 (2)	5.2871 (1)	5.3043 (1)	5.3257 (2)	5.3414 (2)
	V (Å^3)		207.66 (1)	209.45 (1)	211.71 (1)	214.16 (2)	216.29 (1)
	Or[a] (%)		0.015	0.143	0.170	0.225	0.333
	Ca/Eu	x	0.0323 (1)	0.0331 (1)	0.0329 (1)	0.0336 (1)	0.0359 (1)
		z	−0.0093 (1)	−0.0085 (1)	−0.0088 (1)	−0.0081 (1)	−0.0057 (1)
	O1a	x	0.4932 (4)	0.4871 (4)	0.4903 (4)	0.4915 (5)	0.4909 (7)
		z	0.0683 (4)	0.0558 (4)	0.0554 (4)	0.0566 (5)	0.0641 (7)
	O1p	x	0.2904 (3)	0.2890 (3)	0.2910 (3)	0.2924 (4)	0.2941 (5)
		y	0.0302 (3)	0.03393 (3)	0.0366 (3)	0.0354 (4)	0.0355 (5)
		z	−0.2890 (3)	−0.2912 (3)	−0.2895 (3)	−0.2905 (4)	−0.2908 (5)
	R_{WP} (%)		6.77	7.55	8.83	9.65	9.99
	R_B (%)		1.00	1.48	2.85	2.74	2.89
	χ^2 (%)		1.51	1.76	2.26	2.67	2.76
	R_F (%)		1.04	1.58	2.33	2.79	2.82

[a] Or (Orthorhomibicity) = $(a-c)/(c+a)$ (%).

to the Mn^{3+} ion in an octahedral environment. The a axis increases strongly with increasing Sm content (1.9% from $x = 0$ up to $x = 0.4$ for $T_s = 1473$ K) while the other lattice parameters, b and c, have a smaller increase (1.0% and 1.2%, respectively) as can be observed in Fig. 4. The large differences between a and c lattice parameters can be the macroscopic mark of the cooperative Jahn–Teller distortion due to the Mn^{3+} ion in an octahedral environment. The cell volume increases linearly with increasing Sm^{3+} ion content in accordance with Vegard's law (Fig. 4). This variation confirms the achievement of a solid solution $Ca_{1-x}Sm_xMnO_3$ ($0 \le x \le 0.4$) series and the accommodation of Sm^{3+} ion into the perovskite matrix. The introduction of each Sm^{3+} ion changes the valence of one Mn^{4+} ion to the Mn^{3+} state due to charge compensation. The increase in the cell parameters values is caused by an expansion of the octahedral site that overcomes the contraction on the A-site. This can be explained on the basis of the large difference in the ionic radii [34] between Mn^{3+} (0.645 Å) and Mn^{4+} (0.530 Å) in octahedral coordination with oxygen, that overcomes the difference between Ca^{2+} (1.34 Å) and Sm^{3+} (1.24 Å). In fact it can be concluded that the decrease of the A site mean ionic radii (3.0%) is lower than the increase of the B site mean ionic radii (8.7%) as it can be seen in Table 3.

Moreover, the lattice parameters are observed to increase with concomitant raise in the orthorhombicity as the Sm content increases. The system orthorhombicity (Or (%)) has been defined

Table 2
Selected bond distances (Å), angles (°) and D values determined from Rietveld refinements for $Ca_{1-x}Sm_xMnO_3$ ($0 \le x \le 0.4$).

T_s (K)	x	0	0.1	0.2	0.3	0.4
1073	Mn–O1a x2	1.895 (1)	1.897 (3)	1.903 (1)	1.906 (1)	1.915 (1)
	Mn–O1p x2	1.908 (2)	1.922 (2)	1.925 (2)	1.937 (3)	1.958 (3)
	Mn–O1p x2	1.903 (2)	1.909 (2)	1.922 (2)	1.925 (3)	1.928 (3)
	⟨Mn–O$_p$⟩	1.906	1.916	1.924	1.931	1.943
	⟨Mn–Ooct⟩	1.902	1.908	1.915	1.923	1.933
	D[a]	0.994	0.990	0.989	0.987	0.986
	Mn–O1a–Mn	159.71 (2)	159.60 (2)	158.51 (2)	158.25 (3)	158.18 (3)
	Mn–O1p–Mn	158.51 (8)	157.53 (9)	156.57 (9)	156.21 (9)	155.10 (1)
1473	Mn–O1a x2	1.896 (1)	1.896 (1)	1.898 (1)	1.904 (1)	1.914 (1)
	Mn–O1p x2	1.907 (2)	1.919 (2)	1.929 (2)	1.940 (2)	1.952 (3)
	Mn–O1p x2	1.896 (2)	1.904 (2)	1.916 (2)	1.926 (2)	1.938 (3)
	⟨Mn–O$_p$⟩	1.902	1.912	1.924	1.933	1.945
	⟨Mn–Ooct⟩	1.900	1.906	1.915	1.923	1.935
	D[a]	0.998	0.992	0.986	0.985	0.984
	Mn–O1a–Mn	159.48 (2)	159.48 (1)	158.90 (2)	158.69 (2)	158.36 (3)
	Mn–O1p–Mn	157.44 (7)	156.28 (7)	155.46 (8)	155.43 (9)	154.72 (9)

[a] D = Mn–O$_a$/⟨Mn–O$_p$⟩.

Table 3
Ionic composition, mean ionic radii of the A and B sites and the tolerance factor (t) for $Ca_{1-x}Sm_xMnO_3$ ($0 \le x \le 0.4$).

x	$Ca^{2+}_{1-x}Sm^{3+}_{x}Mn^{4+}_{1-x}Mn^{3+}_{x}O_3$	Mean ionic radii (A site – XII) (Å)	Mean ionic radii (B site – VI) (Å)	t
0	$CaMn^{4+}O_3$	1.34	0.530	1.004
0.1	$Ca_{0.9}Sm_{0.1}Mn^{4+}_{0.9}Mn^{3+}_{0.1}O_3$	1.33	0.542	0.994
0.2	$Ca_{0.8}Sm_{0.2}Mn^{4+}_{0.8}Mn^{3+}_{0.2}O_3$	1.32	0.553	0.985
0.3	$Ca_{0.7}Sm_{0.3}Mn^{4+}_{0.7}Mn^{3+}_{0.3}O_3$.	1.31	0.564	0.976
0.4	$Ca_{0.6}Sm_{0.4}Mn^{4+}_{0.6}Mn^{3+}_{0.4}O_3$	1.30	0.576	0.966

by the expression Or (%) = $[(a-c)/(a+c)]\times100$. It is observed an increase from 0.022 to 0.409% and 0.015 to 0.333% for $x = 0$ and $x = 0.4$ respectively for the synthesis temperatures 1073 K and 1473 K (see Table 1). Furthermore, there is a slight decrease in orthorhombicity with increasing synthesis temperature, which is understandable taking into account that with longer times and higher synthesis temperatures the crystallinity of the samples is improved and a better definition of the XRD peak shape is observed. The $Ca_{0.6}Sm_{0.4}MnO_3$ phase shows a large distortion indicated by the large differences between a and c lattice parameters. As referred before this is the macroscopic mark of the cooperative Jahn–Teller distortion due to the Mn^{3+} ion in an octahedral environment. Both, the orthorhombic and the octahedron distortions increase with increasing the Sm content (see Fig. 4 and Tables 1 and 2).

Our data is in agreement with the reported behaviour for the lattice parameters variation with the x value in the $Ca_{1-x}Sm_xMnO_3$ series ($0 \le x \le 0.4$) [14–16,24–27,30]. The calculated lattice parameters values for the $CaMnO_3$ phase also agree well with the data reported in the literature [24–27,30]. In what concerns substituted samples, our data are in agreement with the ones reported earlier for the same phases prepared by high temperature ceramic route (near 1573–1873 K) [14–16]. However, it is important to point out that the heat treatments used in this work are distinct from the published ones.

The tolerance factor, $t = (r_A + r_O)/\sqrt{2}(r_B + r_O)$ (where r_A, r_B, r_O are the radius of ions A, B and O, respectively), which is a quantitative measure of the structural perfection of the ABO_3 perovskites, was calculated using average values for r_A and r_B and are also presented in Table 3. The t values reflect the effects of replacement of Ca^{2+} for Sm^{3+} ions in the $Ca_{1-x}Sm_xMnO_3$ series. Decreasing the Sm content the tolerance factor approaches the ideal value ($t \to 1$) and the tilting of the (MnO_6) octahedra are significantly lower than those observed in the phases containing high concentration of samarium. As mentioned before with the increase in Sm content, the average ion size A site, $\langle r_A \rangle$, decreases by 3.0% and the $\langle r_B \rangle$ increases by 8.7%. Both effects result in a decrease of the tolerance factor by 3.8%. A decrease in t value leads to a significant lowering in the Mn–O–Mn bond angle from 180°. The major effect on t, and therefore in the Mn–O–Mn bond angle, is the increase in the MnO_6 polyhedron size as it can be seen from the average bond lengths of ⟨Mn–O(oct)⟩ octahedra included in Table 2. From this table it can be also detected a systematic change in the values of the bond length and the bond angle with Sm content. The increase in the Mn^{3+} concentration with samarium content increases the average Mn–O distance (⟨Mn–Ooct⟩) in the lattice and also affects the bond angles between neighbouring octahedra. For the $CaMnO_3$ phase ($x = 0$) the Mn–O distances and bond angles are comparable to the corresponding values reported for the same phase [24–26]. For the substituted samples ($x \neq 0$) it is observed that the Mn–O bond lengths show a gradual increase with Sm content, which is consistent with the increase of all cell lattice parameters. This effect is more clearly seen along the a–c basal plane, namely changes in Mn–O1p bonds lengths. The change in the apical-bond length Mn–O1a is much smaller than the a–c basal plane (see Fig. 5). In general, for the unsubstituted sample the octahedral coordination of manganese with oxygen is almost undistorted, with six approximately equal Mn–O distances. For the substituted samples the four Mn–O1p distances, in the a–c plane, become longer than the two Mn–O1a distances along the b axis, since in this case the Jahn–Teller distortion which is due to the Mn^{3+} content mainly affects the equatorial Mn–O1p bonds. As expected the bonds distances variation with the samarium content is very similar to the cell parameters variation. These results clearly demonstrate that there is a close link between the lattice parameters and the presence of the Jahn–Teller distorted $Mn^{3+}O_6$ octahedra with the dz^2 orbital oriented in the a–c plane. The increase in the structure distortion with Sm content is also well visible by the systematic decrease of the octahedral distortion parameter values D, $D = \langle Mn–O_a \rangle / \langle Mn–O_p \rangle$ (Table 2). Moreover, as samarium content increases, the values of Mn–O1a–Mn and Mn–O1p–Mn angles indicate a higher distortion. In fact, for $CaMnO_3$ both angles present similar values, close to 160°, while in the structures where Ca is substituted by Sm, the same angles become significantly different from each other and smaller than 160°.

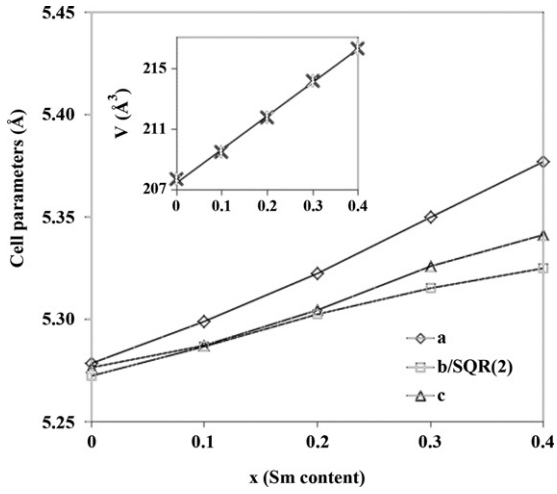

Fig. 4. Evolution of the cell parameters of the *Pnma*-type orthorhombic cell, at room temperature, *vs.* Sm content ($0 \le x \le 0.4$) (T_s = 1473 K). Inset: evolution of the cell volume *vs. x* for $Ca_{1-x}Sm_xMnO_3$ manganites.

3.3. Particle size and morphology

The average crystallite size, D_{hkl}, of the samples prepared at 1073 and 1473 °C was calculated from the main reflection of the orthorhombic unit cell using the Debye–Scherrer equation [29], $D_{hkl} = 0.9\lambda/B\cos\theta$, where λ is the wavelength of Cu Kα radiation, θ the Bragg diffraction angle of the line and B the difference in profile widths of broadened and standard samples (in this study, a silicon standard was used): $B^2 = B^2_M - B^2_S$ where B_M and B_S are the measured widths, at half maximum intensity, of the lines from the sample and the standard, respectively. The crystallite size values for all $Ca_{1-x}Sm_xMnO_3$ samples show great differences between the unsubstituted and substituted calcium manganites for both

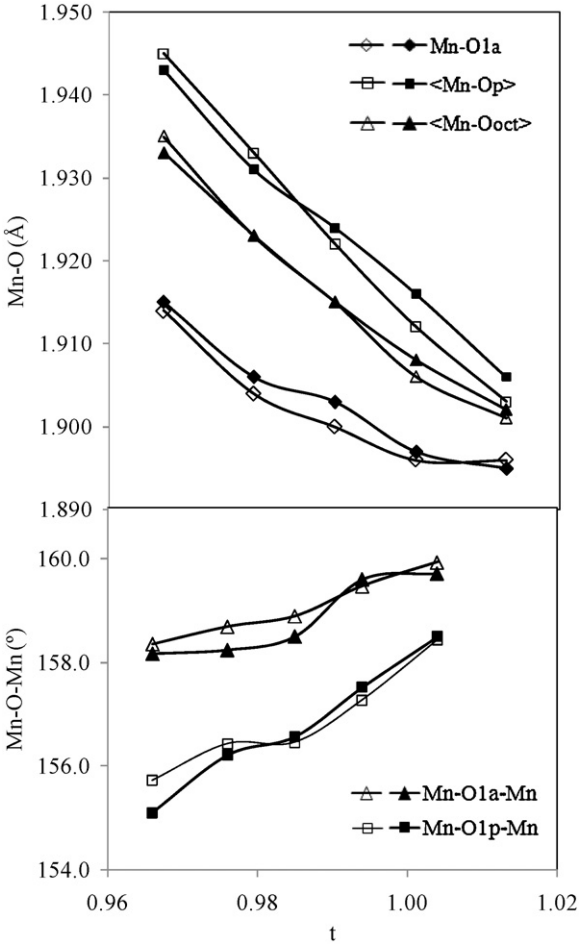

Fig. 5. (a) Average ⟨Mn–O⟩ bond length and (b) ⟨Mn–O–Mn⟩ bond angles as a function of tolerance factor for $Ca_{1-x}Sm_xMnO_3$ ($0 \le x \le 0.4$). Open symbols correspond to T_s = 1473 K and fill symbols to T_s = 1073 K.

synthesis temperatures, i.e., 85 nm for $x = 0$ [26,27] and 42 nm for $x \ge 0.1$ for the samples prepared at 1073 K. For the phases synthesized at 1473 K the crystallite sizes increase to the value of 103 nm for $x = 0$ and 85 nm for $x \ge 0.1$. As expected, the mean crystallite size increases with the increase in annealing temperature. It can be further observed that the samples containing samarium present crystallite sizes smaller than those of the unsubstituted calcium manganites. Moreover, for the substituted calcium manganites the samarium content does not influence the crystallite size because the obtained D_{hkl} values are equal for the different phases synthesized at each synthesis temperature.

These values were further confirmed with the SEM images presented in Fig. 6. As it can be seen there is a significant difference between the grain size of the unsubstituted and substituted samples. The $CaMnO_3$ sample presents particles almost spherical in shape and a size in the range 0.3–0.6 μm [26,27] for T_s = 1073 K and 1–2 μm for T_s = 1473 K. For the substituted manganite samples the morphology is quite similar but the particles size is much smaller (~0.1 μm for T_s = 1073 K and 0.5−1 μm for T_s = 1473 K) than that of the $CaMnO_3$ particles and does not depend on the amount of samarium introduced in the phase. The reduction in particle size with the increase in samarium content leads to an increase in surface area.

From the SEM micrographs of Fig. 6 it is also clear that with the increase of the sintering temperature the grain size increases and the grains become more densely packed, leading to a narrowing of the grain boundary regions. Higher sintering temperatures are expected to yield larger crystallite sizes and reduce strain as compared to the small sized grains. Thus, this strain relaxation with increasing grain size can lead to a reduction in the orthorhombicity of the system as it is observed from the decrease on the O_r values with enhance of T_s presented in Table 1. Moreover, when the grain size becomes larger, the grain-boundary effects will also decrease because of the decrease of grain boundaries. Therefore, the grain-boundary effect should increase from $CaMnO_3$ samples to Sm-substituted phases due to the increase of the width and amount of grain boundaries.

Since all these samples were prepared at the same conditions, it can be concluded that the difference in the crystallite and grain sizes between unsubstituted and substituted samples results mainly from the samarium influence on the grain growth. So, the microstructure indicates that the grain growth decreases, as the Ca is substituted by Sm in the $CaMnO_3$ phase, which leads to an increase of the number of open pores, i.e., porosity. The $CaMnO_3$ phase becomes denser than the Sm-substituted phases and loses porosity.

There are several factors that may be responsible for the nanosize of the resulting powders. In this study, the relatively low formation temperature (1073 K) of $Ca_{1-x}Sm_xMnO_3$ phases as a consequence of the synthesis method should be the greatest contribution to the nanosize powders. In fact, since the reactants are uniformly mixed in solution at atomic or molecular level during combustion, the nucleation process can occur through the rearrangement and short-distance diffusion of nearby atoms and molecules. Moreover, the large volume of the gases developed during the combustion reactions limits the inter-particle contact. i.e., the explosive nature of the combustion leads to the rapid evolution of a large quantity of gaseous products which helps the disintegration of the ashes. Additionally, the combustion process rate is so fast that there is not enough energy and time available for long distance diffusion of the atoms or molecules which would result in crystallites growth. Consequently, the initial powders nanosize is retained after the combustion reaction.

3.4. Fourier transform infrared spectroscopy

Fig. 7 shows the infrared spectra of nanocrystalline $Ca_{1-x}Sm_xMnO_3$ ($0.1 \le x \le 0.4$) prepared at the synthesis temperatures of 1073 and 1473 K. The near-ideal MnO_6 octahedron has the symmetry of the point group, which has six vibrating modes, but only two of them are IR active, i.e., the B cations in the octahedral site of the perovskite structure usually exhibit two IR active modes. The band around 600 cm^{-1} corresponds to the stretching mode, which involves the internal motion of a change in length of the O–Mn–O or Mn–O bonds [31,32]. The band around 400 cm^{-1} is due to the bending mode, which is sensitive to O–Mn–O bond angle. These two bands are related to the surrounding environment of the MnO_6 octahedra. All spectra in Fig. 7 exhibit both absorption bands, although they are less visible for the synthesis temperature of 1473 K. This may be related to the electrical behaviour exhibited by the $Ca_{1-x}Sm_xMnO_3$ ($0.1 \le x \le 0.4$) series since, according to Ganguly et al. [35], in compounds with metallic character, may arise decrease in the polarity of the Mn–O bonds, as a result of electronic delocalization in these bonds and, for very small values of electrical resistivity, a change can occur or even the disappearance of the vibration modes of MnO_6 octahedra.

From the spectra in Fig. 7 it can be further noticed that the compounds containing samarium show a shift of the higher frequency band from ~570 to ~585 cm^{-1} for both sintering temperatures. This shift is more pronounced for T_s = 1473 K and results from the reduction of the Mn^{4+} to Mn^{3+} ions in the samples with increasing samarium content. It can also be detected that the lower frequency band, corresponding to the bending mode, did not change.

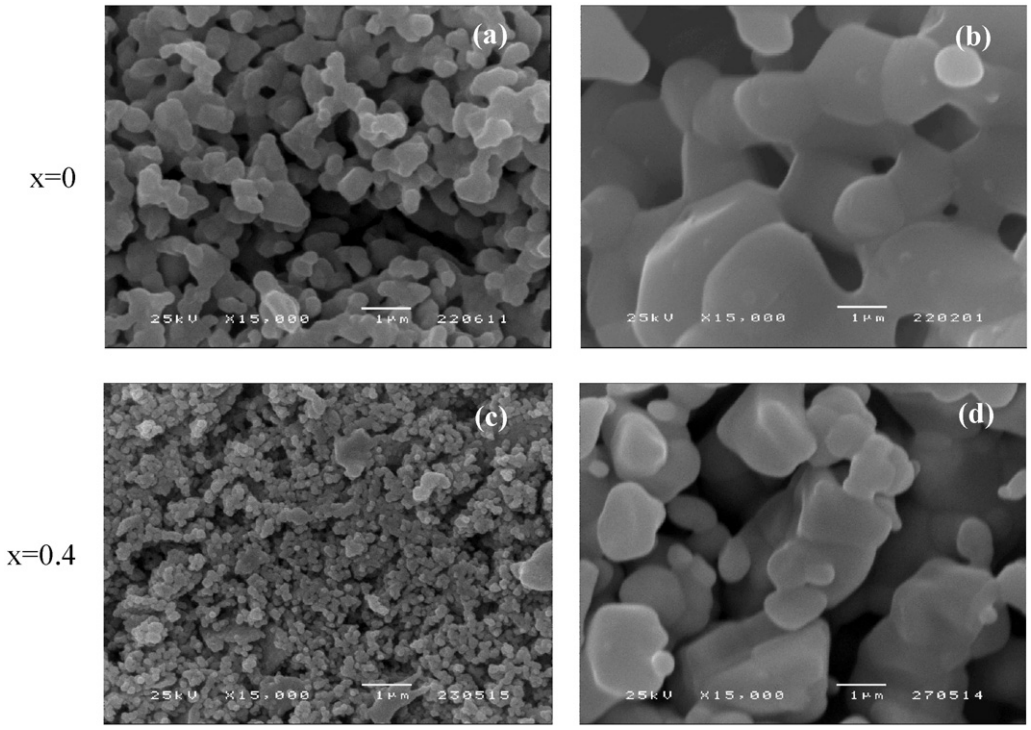

Fig. 6. Scanning electron micrographs of $Ca_{1-x}Sm_xMnO_3$ manganites: (a and c) T_S = 1073 K; (b and d) T_S = 1473 K.

3.5. High temperature resistivity measurements

The temperature dependence of electrical resistivity from 300 K up to 900 K for $Ca_{1-x}Sm_xMnO_3$ samples is depicted in Fig. 8. The analysis of this figure clearly shows that, for both synthesis temperatures, the partial substitution of calcium by samarium rapidly lowers the electrical resistivity by several orders of magnitude in comparison with $CaMnO_3$. The huge difference in the electrical resistivity between the parent $CaMnO_3$ and $Ca_{1-x}Sm_xMnO_3$ ($0.1 \leq x \leq 0.4$) samples can be attributed to the changes of Mn^{4+}/Mn^{3+} ratio. The pure compound $CaMnO_3$ contains only Mn^{4+} ions and has no e_g electrons. By doping electrons with trivalent rare-earth ions, e_g levels become occupied as the Mn^{3+} ions are created. So the electron hopping between Mn^{3+} and Mn^{4+} can be responsible for the relatively low electrical resistivity exhibited by the substituted phases. The presence of an appreciable concentration of Mn^{3+} introduces a large number of charge carriers (electrons) and facilitates the movement of those charge carriers by hopping mechanism. Moreover, similar variation can be observed in the room temperature resistivity ($\rho_{300\,K}$) values (Table 4 and Fig. 8), i.e., the substituted samples show $\rho_{300\,K}$ much smaller than the unsubstituted phase.

Also, for the phases prepared at T_S = 1073 K, the electrical resistivity decreases with increase in temperature, indicating that all the samples present a semiconducting nature, i.e., exhibit a classical semiconducting behaviour with a negative temperature coefficient of resistivity ($d\rho/dT < 0$) for the temperature range investigated. Comparable results are reported by other authors for $Ca_{1-x}R_xMnO_3$ system (R = Ho, Eu, $0 \leq x \leq 0.4$) [26,27,30].

For T_S = 1473 K, the behaviour of the Sm-substituted phases is much different. The $\rho(T)$ curves show a metal–insulator transition for all substituted phases ($0.1 \leq x \leq 0.4$) marked by the presence of a broad peak in the resistivity curves since the signal of $d\rho/d$T changes from negative to positive in the temperature range of 300–900 K. Above the transition temperature, T_{MI}, the electrical resistivity of $Ca_{1-x}Sm_xMnO_3$ ($0.1 \leq x \leq 0.4$) has a slight positive temperature coefficient as evidenced in Fig. 8b revealing a metallic behaviour. It can be observed that, with the increase in Sm content T_{MI}, determined from the inflection point, increases from 430 K for x = 0.1 up to 629 K for x = 0.4 (see Fig. 8b and Table 4). The samples with x = 0.4 and 0.3 show a slope change at the metal–insulator transition, exhibiting a broad peak transition, while the phases with x = 0.1 and 0.2 display a significantly smaller increase in the resistivity upon cooling below the transition. However it is observable a trend to reach a semimetallic state below 400–450 K. Thus, it can be concluded that all substituted samples exhibit metallic behaviour by cooling from 900 K reaching a temperature (that depends on the substitution level) where the resistivity begins to

Table 4
Metal–insulator transition temperature (T_{MI}), room temperature resistivity ($\rho_{300\,K}$), activation energie (E_a) and valence state of Mn^{x+} ions for $Ca_{1-x}Sm_xMnO_3$ ($0 \leq x \leq 0.4$).

x	Mn^{x+}	T_s = 1073 K				T_s = 1473 K				
		$\rho_{300\,K}$ (Ω cm)	Wr	Temperature range used for obtaining E_a (K)	E_a (meV)	$\rho_{300\,K}$(Ω cm)	Wr	T_{MI} (K)	Temperature range used for obtaining E_a (K)	E_a (meV)
0	4.0	5.453	1	300–600 625–900	51 394	2.12	1	–	300–900	127
0.1	3.9	0.269	0.9853	300–900	102	0.017	0.9850	430	300–430	36
0.2	3.8	0.291	0.9658	300–900	104	0.017	0.9641	498	300–498	49
0.3	3.7	0.366	0.9497	300–900	116	0.030	0.9492	618	300–618	69
0.4	3.6	0.420	0.9285	300–900	130	0.090	0.9252	629	300–629	79

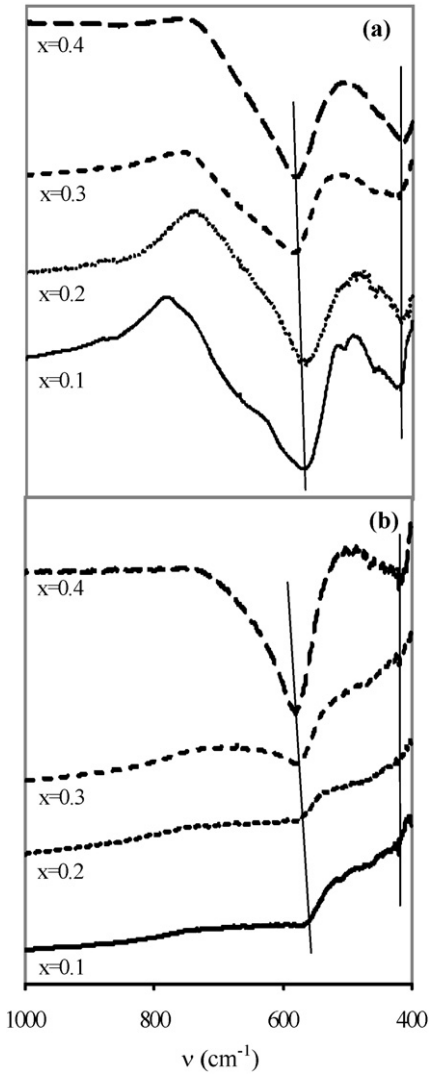

Fig. 7. Infrared spectra of $Ca_{1-x}Sm_xMnO_3$ ($0 \le x \le 0.4$) samples: (a) T_s = 1073 K and (b) T_s = 1473 K.

increase. Below T_{MI} the samples exhibit semiconductor behaviour. The trends followed by the present data for the high temperature resistivity of $Ca_{1-x}Sm_xMnO_3$, namely the observation of T_{MI}, are analogous to previous reports on ($Ln_{1-x}Ca_xMnO_3$) (Ln = La, Nd, Ga, Tb, Ho, Y) [36–39] and $Ca_{1-x}R_xMnO_3$ system (R = Ce, Ho) [24,25]. These manganites exhibit a metal–insulator transition at high temperature which was explained by the energy band scheme for the perovskite-type structure proposed by Goodenough [40]. Accordingly the increase in Mn–O distance enhances the magnitude of the electrostatic field and consequently the transition temperature is raised. In this work this variation is entirely observed with increasing Mn–O distance. The $Ca_{0.9}Sm_{0.1}MnO_3$ phase exhibits identical behaviour to the published recently by Wang et al. [16] for the same phase prepared by traditional solid-state reaction method at 1623 K, although they have obtained a T_{MI} value slightly lower (T_{MI} = 365 K) than the one obtained in the present work. Below T_{MI} the samples present semiconductor behaviour; this is in agreement with the studies reported by other authors [13–15,17,18,41] for the electron-doped $Ca_{1-x}Sm_xMnO_3$ ($x \le 0.4$) samples for temperatures lower than 300 K.

According to the literature [7,12,41–45] the MI transition can be attributed to the charge-ordering phenomena (CO), i.e., the ordering of the Mn^{3+} and Mn^{4+} species over the manganese lattice. In this case, the onset of the CO is coincident with an increase on the electrical resistivity and is typical of many types of CO systems.

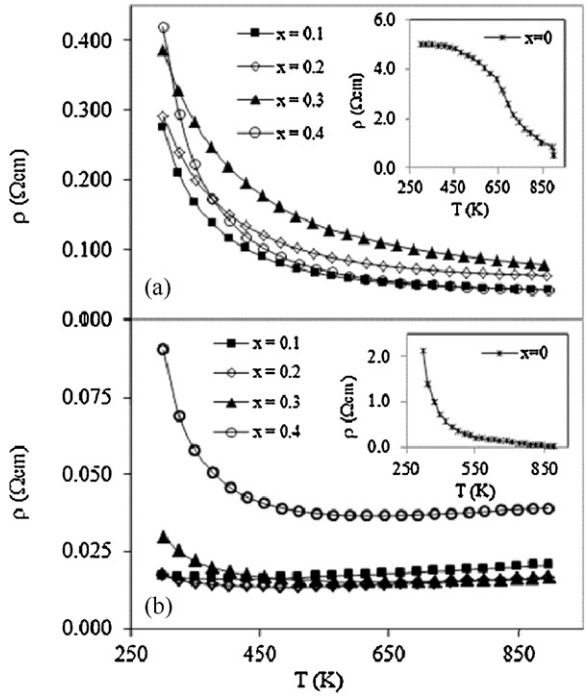

Fig. 8. Temperature dependence of the electrical resistivity for $Ca_{1-x}Sm_xMnO_3$ ($0 \le x \le 0.4$) prepared at (a) 1073 K and (b) 1473 K. The inset shows the ρ *vs.* T of $CaMnO_3$.

As mentioned before, for the electron-substituted samples prepared at 1073 K it is observed the disappearance of the MI transition. This can be due to the grain size variation as a consequence of the difference in heat treatments of the samples where shorter times and lower temperature were used. These shorter treatments promote the short range ordering of the Mn^{3+} and Mn^{4+} species. So, decreasing significantly the synthesis temperature this charge-ordering phenomenon can disappear and also the MI transition.

Moreover, the substituted samples show ρ values at room temperature ($\rho_{300\,K}$) much smaller than those of the unsubstituted sample. It is known that the electrical conductivity depends on the microstructure of the specimen and on the Mn^{4+}/Mn^{3+} ratio. Consequently this change can be due to the increase in the Mn^{3+}concentration with calcium substitution which overcomes the effect of the decrease in the grain size of the substituted sample. On the other hand, the $\rho_{300\,K}$ values slightly increase with Sm content. The highest electrical conductivity occurs for $Ca_{0.6}Sm_{0.4}MnO_3$ sample and this can be justified by the decrease in the valence state of Mn with calcium substitution (from $Mn^{3.9+}$ for x = 0.1 to $Mn^{3.6+}$ for x = 0.4). The ($\rho_{300\,K}$) values obtained for the Sm-substituted samples prepared at T_s = 1473 K agree with the ones reported in the literature for similar samples [15–18,41], although slightly higher values have been obtained for the room temperature resistivity.

For $Ca_{1-x}Sm_xMnO_3$ ($0 \le x \le 0.4$) with the same composition and prepared at two distinct sintering temperatures the sensitivity of electrical resistivity to grain boundaries is strong and it is nearly one order of magnitude lower for samples synthesized at 1473 K than for samples prepared at 1073 K.

The effective e_g bandwidth W, determined by the overlapping between Mn 3d and O 2p orbitals, which is strongly affected by structural distortions, has been calculated from XRD refinement data. For the orthorhombic perovskites, within the tight-binding approximation, W is represented by $W \approx \cos[180^\circ - \langle Mn–O–Mn \rangle]/2d^{3.5}_{Mn-O}$ [46]. The values of relative

bandwidth $Wr(= W_{Ca_{1-x}Sm_xMnO_3}/W_{CaMnO_3})$ are listed in Table 4. $Ca_{0.9}Sm_{0.1}MnO_3$ exhibits the maximum Wr due to the smallest $\langle d_{Mn-O}\rangle$ and moderate ⟨Mn–O–Mn⟩. Since the conduction is governed by e_g electrons, the enhancement of the effective e_g bandwidth leads to a decrease on the system electrical resistivity. Therefore, one can find that the variation of $\rho_{300\,K}$ with Sm^{3+} doping is approximately reverse to Wr; $Ca_{0.9}Sm_{0.1}MnO_3$ exhibits the lowest resistivity, corresponding to its largest e_g bandwidth. Additionally, the slight difference in bandwidth induced by structural distortions gives rise to the different resistivities of the samples, even though they have almost equal electron carrier concentration.

In the present study was also found that the polycrystalline compounds synthesized at 1473 K exhibit very low electrical resistivity values compared with the ones corresponding to the samples prepared at 1073 K. This large variation in the electrical behaviour could be due to the different annealing treatments which induce an important change in the crystallite and grain sizes, as evidenced by SEM and the comparison of the D_{hkl} values (see Fig. 6). It can be considered that the increase of ρ with the reduction of grain size is mainly related to the increase of both the height and width of tunneling barriers. Evidently, with the grain size decreasing the number of pores and consequently, the porosity increase. The increase of ρ with the grain size decrease is a result of carriers sampling and more grain boundary material. The large volume of grain boundary material produces a greater electrical conductivity change. In these cases, the influence on the electrical transport properties of the mixed valence manganese ions is less important. In fact, it was found [47–49] that for fine-particle perovskite manganites, an increase in resistivity occurs as the particle size decreases and the grain boundary contribution increases due to the broken Mn–O–Mn bonds at the surface of the smaller particles that impede the conduction. This is a typical behaviour in the case of nanoparticles of the manganite system [47,50].

In addition, it is well known that the mechanism of electrical conduction in (Ca,R)MnO_3 (R = Ce, Ho, Eu, Sm) is by hopping of polarons [12,16,24–27,30]. For conduction to occur, $Mn^{3+}$and Mn^{4+} should be the nearest neighbours and the electron jumps from Mn^{3+} to Mn^{4+}must be via O^{2-} (i.e. Mn^{3+}–O–Mn^{4+} bonding). As a consequence the activation energy of total conduction can be evaluated using the Arrhenius equation

$$\sigma = \left(\frac{A}{T}\right)\exp\left(\frac{-E_a}{kT}\right) \quad (1)$$

where σ is the conductivity, A the pre-exponential factor, k the Boltzmann's constant, T the absolute temperature and E_a the activation energy of conduction. Using Eq. (1) the activation energy of conduction values were estimated from the slope of the linear portion of $\log(\sigma T)$ *vs.* $1/T$ (see Fig. 9) and are shown in Table 4. The activation energies obtained for $Ca_{1-x}Sm_xMnO_{3-\delta}$ ($0 \le x \le 0.4$) series are fairly low and for substituted samples increase monotonically with Sm content (Table 3) for both sintering temperatures. The substitution of $Ca^{2+}$for Sm^{3+} leads to a higher Mn^{3+} content and, as a consequence, the lowering of the energy barrier for polaron hopping, which lowers the activation energy for conduction from $x = 0$ to $0.1 \le x \le 0.4$. As mentioned earlier [20,51], some authors verified that the activation energy values increase with decreasing grain size. In fact, increasing grain size the interconnectivity between grains increases, which enhances the possibility of conduction electrons to hop to the neighboring sites, thereby decreasing the E_a value. Furthermore, for the Sm-substituted samples the activation energy increases slightly with samarium content, which can be linked to the increase of structural distortions, owing to the enhancement of energy barrier for polaron hopping.

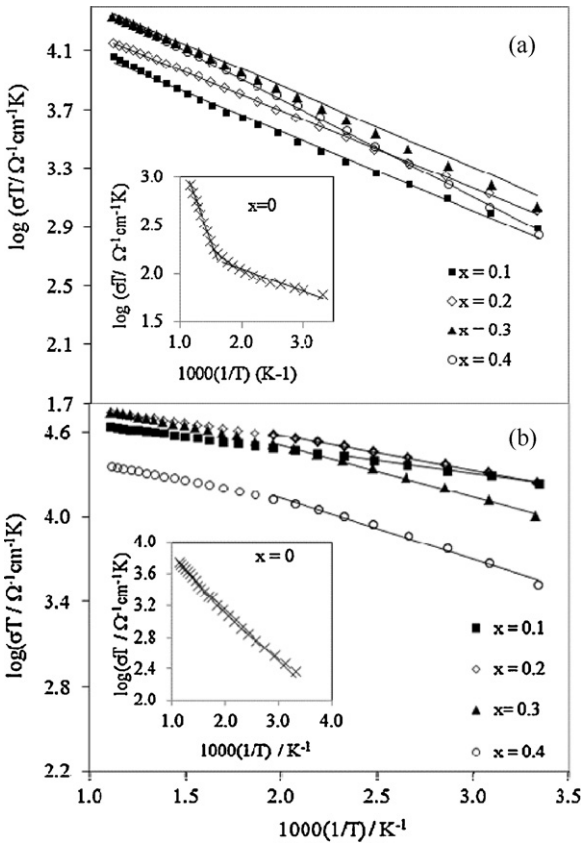

Fig. 9. Plot of $\log(\sigma T)$ *vs.* $1000/T$ for $Ca_{1-x}Sm_xMnO_3$ ($0 \le x \le 0.4$) prepared at (a) 1073 K and (b) 1473 K. The inset shows the ρ *vs.* T of $CaMnO_3$.

4. Conclusions

Nanopowders of $CaMnO_3$ and Sm-substituted (Ca,Sm)MnO_3 with different samarium content were prepared by Pechini method, via auto-combustion, at low temperature (1073 K) and shorter heating treatments when compared to the conventional ceramic route. The process was reproducible for the generation of powder particles with nearly uniform shape, size and composition. XRD and SEM analyses of calcined powders confirmed the nanometric size and phase purity. By changing the sintering temperature, it was possible to change the growth of grain size. However, it was revealed that the samarium content has no effect on grain growth. The determination of the Mn–O–Mn bond angles and Mn–O bond lengths for the samples with different particle sizes, from Rietveld analysis, enabled to explain such contrasting behaviour.

Infrared spectroscopy revealed that both unsubstituted and Sm-substituted calcium manganites show two IR active vibrational modes near 400 and 600 cm^{-1} corresponding to the O–Mn–O bending and Mn–O stretching mode. The profile bands are slightly influenced by the sintering temperature and the differences may be related to the electrical behaviour exhibited by the $Ca_{1-x}Sm_xMnO_3$ ($0.1 \le x \le 0.4$) series.

Concerning the electrical transport properties of partially substituted $CaMnO_3$-based perovskite-type oxides all samples for $T_s = 1073$ K exhibit a semiconducting nature and the substitution of Ca^{2+} by Sm^{3+} causes a marked increase in the electrical conductivity when compared with $CaMnO_3$. This tendency can be attributed, at least partly, to an increase on the carrier concentration caused by the substitution effect of the higher valence cations, which induces changes in the Mn^{3+} to Mn^{4+} ratio.

For $T_s = 1473$ K the samples show much lower electrical resistivity values and, for Sm containing samples, a MI transition

temperature was observed. By decreasing the grain size the electrical resistivity increases and the MI transition disappears.

Moreover, the A-site substitution systematically studied in this work has brought out the importance of the carrier density (n) and structural effects, quantified by the average Mn–O bond length ($\langle$Mn–O$\rangle$) and the average Mn–O–Mn bond angle, in controlling the physical properties of the manganites.

References

[1] R. von Helmot, J. Wecker, B. Holzapfel, L. Schultz, K. Samwer, Phys. Rev. Lett. 71 (1993) 2331–2333.
[2] R. Mahesh, R. Mahendiran, A.K. Raychaudhuri, C.N.R. Rao, J. Solid State Chem. 114 (1995) 297–299.
[3] A.J. Millis, P.B. Littlewood, B.I. Shraiman, Phys. Rev. Lett. 74 (1995) 5144–5147.
[4] C.N.R. Rao, A.P.N. Santosh, A.K. Cheetham, Chem. Mater. 10 (1998) 2714–2722.
[5] Y. Tomioka, T. Okuda, Y. Okimoto, A. Asamitsu, H. Kuwahara, Y. Tokuraa, J. Alloys Compd. 326 (2001) 27–35.
[6] G.H. Zheng, Z.X. Dai, Y.Y. Zhang, Y.P. Sun, J. Alloys Compd. 489 (2010) 348–352.
[7] H. Chiba, M. Kikuchi, K. Kusaba, Y. Muraoka, Y. Syono, Solid State Commun. 99 (1996) 499–502.
[8] A. Maignan, C. Martin, F. Damay, B. Raveau, Chem. Mater. 10 (1998) 950–954.
[9] J. Blasco, C. Ritter, J. Garcia, J.M. de Teresa, J. Pérez–Cacho, M.R. Iharra, Phys. Rev. B 62 (2000) 5609–5618.
[10] Z. Zeng, M. Greenblatt, M. Croft, Phys. Rev. B63 (2001), 224410-1-224410-10.
[11] S. Bošković, J. Dukić, B. Matović, Lj. Živković, M. Vlajić, V. Krstić, J. Alloys Compd. 463 (2008) 282–287.
[12] H. Muguerra, B. RivasMuriasa, M. Traianidis, C. Marchal, Ph. Vanderbemden, B. Vertruyena, C. Henrist, R. Cloots, J. Alloys Compd. 509 (2011) 7710–7716.
[13] C. Martin, A. Maignan, F. Damay, M. Hervieu, B. Raveau, J. Solid State Chem. 134 (1997) 198–202.
[14] P. Laffez, M. Zaghrioui, L. Reversat, P. Ruello, Appl. Phys. Lett. 89 (2006), 081909-1-081909-3.
[15] M. Hervieu, A. Barnab, C. Martin, A. Maignan, F. Damay, B. Raveau, Eur. Phys. J. B 8 (1999) 31–41.
[16] Y. Wang, Y. Sui, W. Su, J. Appl. Phys. 104 (2008), 093703-1-093703-7.
[17] C. Martin, A. Maignan, M. Hervieu, B. Raveau, Z. Jiraĭk, M.M. Savosta, A. Kurbakov, V. Trounov, G. André, F. Bourée, Phys. Rev. B 62 (2000) 6442–6449.
[18] A. Maignan, C. Martin, F. Damay, B. Raveau, J. Hejtmanek, Phys. Rev. B 58 (1998) 2758–2763.
[19] S.K. Jaiswal, J. Kumar, J. Alloys Compd. 509 (2011) 3859–3865.
[20] A. Chaouchi, S. Kennour, S. d'Astorgb, M. Rguiti, C. Courtois, S. Marinel, M. Aliouat, J. Alloys Compd. (2010), doi:10.1016/j.jallcom.2011.06.085.
[21] A.Z. Simões, R.F. Pianno, E.C. Aguiar, E. Longo, J.A. Varela, J. Alloys Compd. 479 (2009) 274–279.
[22] A.Z. Simões, F.G. Garcia, C.S. Riccardi, J. Alloys Compd. 493 (2010) 158–162.
[23] M. Popa, M. Jose, C. Moreno, J. Alloys Compd. 509 (2011) 4108–4116.
[24] M.E. Melo Jorge, M.R. Nunes, R. Silva Maria, D. Sousa, Chem. Mater. 17 (2005) 2069–2075.
[25] D. Sousa, M.R. Nunes, C. Silveira, I. Matos, A.B. Lopes, M.E. Melo Jorge, Mater. Chem. Phys. 109 (2008) 311–319.
[26] C. Silveira, M.E. Lopes, M.R. Nunes, M.E. Melo Jorge, Solid State Ionics 180 (2010) 1702–1709.
[27] P.H. Isasi, M.E. Lopes, M.R. Nunes, M.E. Melo Jorge, J. Phys. Chem. Solids 70 (2009) 405–411.
[28] J. Rodriguez-Carvajal, Fullprof version 1.8a–May 2002, ILL, unpublished.
[29] B.D. Cullity, Elements of X-ray Diffraction, 2nd edition, Addison-Wesley, Reading, MA, 1978.
[30] M.E. Melo Jorge, A. Correia dos Santos, M.R. Nunes, Int. J. Inorg. Mat. 3 (2001) 915–921.
[31] J.T. Last, Phys. Rev. 105 (1957) 1740–1750.
[32] Anthony Arulraj, C.N.R. Rao, J. Solid State Chem. 145 (1999) 557–563.
[33] J.B. Goodenough, L.M. Longo, Crystallographic and magnetic properties of perovskite and perovskite-related compounds, Landolt-Bornstein Tabellen, New Series III/4a, Springer-Verlag, Berlin, 1970.
[34] R.D. Shannon, Acta Cryst. A32 (1976) 751–767.
[35] P. Ganguly, N.Y. Vasanthacharya, J. Solid State Chem. 61 (1986) 164–170.
[36] H. Taguchi, M. Nagao, M. Shimada, J. Solid State Chem. 76 (1988) 284–289.
[37] H. Taguchi, M. Nagao, M. Shimada, J. Solid State Chem. 82 (1989) 8–13.
[38] T. Kobayashi, H. Takizawa, T. Endo, T. Sato, M. Shimada, H. Taguchi, M.J. Nagao, J. Solid State Chem. 92 (1991) 116–129.
[39] H. Taguchi, M. Shimada, J. Solid State Chem. 63 (1986) 290–294.
[40] J.B. Goodenough, J. Appl. Phys. 37 (1966) 1415–1422.
[41] J. Hejtmanek, Z. Jirak, M. Maryško, C. Martin, A. Maignan, M. Hervieu, B. Raveau, Phys. Rev. B 60 (1999) 14057–14065.
[42] Wei Bao, J.D. Axe, C.H. Chen, S.-W. Cheong, Phys. Rev. Lett. 78 (1997) 543–546.
[43] Y. Murakami, D. Shindo, H. Chiba, M. Kikuchi, Y. Syono, Phys. Rev. B 55 (1997) 15043–15047.
[44] E.N. Caspi, M. Avdeev, S. Short, J.D. Jorgensen, M.V. Lobanov, Z. Zeng, M. Greenblatt, P. Thiyagarajan, C.E. Botez, P.W. Stephens, Phys. Rev. B 69 (2004), 104402-1-104402-17.
[45] A. Barnabé, M. Hervieu, C. Martin, A. Maignan, B. Raveau, J. Mater. Chem. 8 (1998) 1405–1411.
[46] M. Medarde, J. Mesot, P. Lacorre, S. Rosenkranz, P. Fischer, K. Gobrecht, Phys. Rev. B 52 (1995) 9248–9258.
[47] L.I. Balcells, J. Fontcuberta, B. Martínez, X. Obradors, Phys. Rev. B 58 (1998) R14697–R14700.
[48] R. Mahesh, R. Mahendiran, A.K. Raychaudhuri, C.N.R. Rao, Appl. Phys. Lett. 68 (1996) 2291–2293.
[49] P.K. Siwach, R. Prasad, A. Gaur, H.K. Singh, G.D. Varma, O.N. Srivastava, J. Alloys Compd. 443 (2007) 26–31.
[50] J. Rivas, L.E. Hueso, A. Fondado, F. Rivadulla, M.A. Lopez-Quintela, J. Magn. Magn. Mater. 221 (2000) 57–62.
[51] Aritra Banerjee, Sudipta Pal, S. Bhattacharya, B.K. Chaudhuri, J. Appl. Phys. 91 (2002), 5215–5134.